Nanotopography modulates cytoskeletal organization and dynamics during T cell activation

Brittany A. Wheatley[a,b,†], Ivan Rey-Suarez[c,†], Matt J. Hourwitz[d], Sarah Kerr[e], Hari Shroff[f], John T. Fourkas[c,d,g], and Arpita Upadhyaya[c,h,*]
[a]Department of Integrative Structural and Computational Biology and [b]Skaggs Graduate School of Chemical and Biological Sciences, The Scripps Research Institute, Jupiter, FL 33458; [c]Institute for Physical Science and Technology; [d]Department of Chemistry and Biochemistry, [g]Maryland Quantum Materials Center, and [h]Department of Physics, University of Maryland, College Park, MD 20742; [e]Department of Physics, University of Colorado, Boulder, CO 80302; [f]National Institute of Biomedical Imaging and Bioengineering, National Institutes of Health, Bethesda, MD 20892

ABSTRACT Exposure to MHC-antigen complexes on the surface of antigen-presenting cells (APCs) activates T cells, inducing the formation of the immune synapse (IS). Antigen detection at the APC surface is thus a critical step in the adaptive immune response. The physical properties of antigen-presenting surfaces encountered by T cells in vivo are believed to modulate T cell activation and proliferation. Although stiffness and ligand mobility influence IS formation, the effect of the complex topography of the APC surface on this process is not well understood. Here we investigate how nanotopography modulates cytoskeletal dynamics and signaling during the early stages of T cell activation using high-resolution fluorescence microscopy on nanofabricated surfaces with parallel nanoridges of different spacings. We find that although nanoridges reduce the maximum spread area as compared with cells on flat surfaces, the ridges enhance the accumulation of actin and the signaling kinase ZAP-70 at the IS. Actin polymerization is more dynamic in the presence of ridges, which influence the directionality of both actin flows and microtubule (MT) growth. Our results demonstrate that the topography of the activating surface exerts both global effects on T cell morphology and local changes in actin and MT dynamics, collectively influencing T cell signaling.

INTRODUCTION

The detection of antigens presented on the surfaces of antigen-presenting cells (APCs) by T cells triggers the T cell activation response to infection (Huppa and Davis, 2003). T cells scan the surface of APCs using small, dynamic actin-dependent protrusions (Cai *et al.*, 2017). T cell receptor (TCR) engagement with peptides bound to major histocompatibility complexes (MHCI or -II) on the surface of APCs activates the TCR and triggers a signaling cascade, inducing actin remodeling. The resulting actin dynamics increase the signaling response to the antigen and leads to T cell spreading on the APC, forming a contact zone known as the immunological synapse (IS). At early stages of activation, actin dynamics support the formation of TCR-associated signaling microclusters by removing diffusive barriers. As the IS matures, actin flows drive signaling microclusters toward the center of the contact zone (Yi *et al.*, 2012; Murugesan *et al.*, 2016), where signaling is down-regulated (Mossman *et al.*, 2005; Babich *et al.*, 2012; Jankowska *et al.*, 2018). IS formation, maturation, and signaling regulation are associated with distinct patterns of actin remodeling.

The two-dimensional (2D) nature of the IS is particularly well suited for studies on planar substrates (stimulatory anti-CD3-coated glass and supported lipid bilayers), facilitating the use of

high-resolution fluorescence microscopy techniques. Such studies have highlighted the existence of multiple dynamic actin networks that are organized by distinct actin nucleators with distinct functional outcomes (Murugesan *et al.*, 2016; Hong *et al.*, 2017). These actin networks play a key role in integrating mechanical and biochemical signals at the IS and thereby function as mechanosensors. The relationship among actin dynamics, TCR signaling, and mechanotransduction at the IS has largely been examined in the context of substrate stiffness (O'Connor *et al.*, 2012; Bashour *et al.*, 2014; Hui *et al.*, 2014) and receptor mobility (Hsu *et al.*, 2012; Ketchum *et al.*, 2014). However, the microenvironment encountered by T cells in vivo is topographically complex due to a variety of actin-mediated protrusions of APCs (Szakal *et al.*, 1985; El Shikh *et al.*, 2007), with features that have radii of curvature on the order of 100 to 300 nm (Felts *et al.*, 2010). Several studies have shown that nanoscale feature substrates alter the actin organization and dynamics in adherent (reviewed in Lou *et al.*, 2018) and immune cells (Galic *et al.*, 2012; Ketchum *et al.*, 2018). How such dynamics facilitate the integration of topographic and antigenic stimuli to influence TCR mediated signaling is unknown.

The microtubule (MT) cytoskeleton also polarizes during T cell activation. Repositioning of the MT-organizing center (MTOC) toward the APC is a hallmark of T cell activation and is required for sustained signaling (Martín-Cófreces *et al.*, 2008). MTOC translocation typically occurs within 3 to 6 min of TCR activation (Yi *et al.*, 2013). The repositioning of the centrosome facilitates the recycling of TCR and LAT (linker for activation of T cells) protein through vesicle delivery and the secretion of signaling molecules, such as interleukin-2 (Martín-Cófreces *et al.*, 2008; Huse *et al.*, 2013; Ritter *et al.*, 2015; Bustos-Morán *et al.*, 2017), as well as through directed delivery of lytic granules toward target cells in cytotoxic T lymphocytes. When the centrosome is properly relocated to the IS, MT filaments grow radially outward. In contrast with the F-actin distribution, the concentration of MTs gradually decreases from the center of a cell to its edge, and MT growth dynamics regulate actin retrograde flow and force generation during signaling activation (Hui and Upadhyaya, 2017; Rey-Suarez *et al.*, 2021). However, little is known about MT dynamics during T cell activation and how these dynamics contribute to mechanosensing and mechanotransduction of substrate topography is unclear.

It is believed that the efficacy of signal transduction downstream of the TCR is optimized to the morphological properties of the T cell/APC contact interface (Upadhyaya, 2017). Exploring this relationship between structure and function is challenging, however, because the T cell/APC interface has intricate, three-dimensional (3D) architectures that are difficult to reconstitute in controlled environments. Here we use nanofabrication and high-resolution imaging to investigate how the topography of the activating surface modulates T cell cytoskeletal dynamics during the early stages of the formation of the IS. We demonstrate that substrate features have global effects on T cell morphology and induce local changes in actin and MT dynamics, collectively influencing T cell signaling.

RESULTS
Nanotopographic surfaces affect T cell spreading during signaling activation
Periodic nanotopographic surfaces coated with stimulatory antibody (anti-CD3) provided the opportunity to obtain systematic data on cytoskeletal dynamics during T cell activation. We used multiphoton absorption polymerization (MAP) (Driscoll *et al.*, 2014; Sun *et al.*, 2015, 2018) (see *Materials and Methods*) to design and fabricate parallel nanoridges of fixed height (~600 nm) and width

(~200 nm) with spacing of 1, 1.8, 3, or 5 µm (Figure 1a). The nanopatterned substrates induced the spreading and activation of Jurkat T cells upon contact. Cells were activated on these surfaces, fixed at specific time points, and imaged with instant structured illumination microscopy (iSIM) (York *et al.*, 2013), as shown in Figure 1b, or imaged live using total internal reflection fluorescence (TIRF) microscopy, as shown in Figure 1c. Cells expressing TagRFP-T-actin and EGFP-EB3, an MT end-binding protein, were activated and allowed to spread on nanotopographic surfaces with varying ridge spacings, and live-cell imaging (Figure 1c and Supplemental Figure S1a) was used to visualize the effects of topography on cell spreading and cytoskeletal dynamics during signaling activation. Time-lapse movies were acquired at 3-s intervals, and the cell contour and contact area were determined from the location of actin fluorescence (see *Materials and Methods*). Analysis of cell contours showed that cell morphology is influenced by the presence of nanoridges (Figure 1d and Supplemental Figure S1b). Cells that were deposited on flat (unpatterned) regions of the substrates spread in a radially symmetric manner, whereas cells contacting the patterned regions of the substrate spread less symmetrically, either along (Figure 1d, top panel) or across the ridges (Figure 1d, middle panel). Both of these types of spreading were observed on all ridge spacings with roughly equal probability.

Cells spreading on patterned surfaces displayed significantly more elongated shapes than cells spreading on flat surfaces, as measured by the eccentricity (see *Materials and Methods* and Supplemental Figure S1c) of the contact region of fixed cells (Figure 1e). We obtained the spreading rate by fitting the time dependence of the spread area to the function $A(t) \sim A_0 \tanh(\delta t)$ (Lam Hui *et al.*, 2012), where A_0 is the final area and δ is the spreading rate (Supplemental Figure S1d). We found that nanoridges did not affect the spreading rate (Supplemental Figure S1e) for any of the ridge spacings investigated. However, A_0 was significantly larger for cells on flat surfaces than for cells on nanoridges (Supplemental Figure S1f). To corroborate this observation, we measured the spread area of cells fixed after 6 min of activation (the time at which maximal spreading is achieved by most cells). Consistent with the results from live cells, we found that the spread area was the smallest for the smallest ridge spacing and was largest on flat surfaces (Figure 1f). To isolate the effect of topography and activation on spreading, we quantified the spread area of cells spreading on patterned surfaces coated with nonstimulatory poly L-lysine (PLL) alone. We found that the spread area of cells was smaller on PLL-coated surfaces compared with activated surfaces for all spacings. Interestingly, cells spreading on 3 and 5 µm PLL-coated surfaces showed an increased spread area compared with narrower spacings and flat nonstimulatory surfaces (Supplemental Figure S1g), suggesting that these ridge spacings might facilitate cell spreading in the absence of stimulation.

Nanotopography influences actin and ZAP-70 distributions in activated T cells
To visualize the F-actin distribution induced by nanopatterns, we fixed cells at the time of maximal spreading (6 min), labeled F-actin using rhodamine-phalloidin staining, and imaged with iSIM (Figure 2, a and d). We found significant accumulation of F-actin along either side of the nanoridges, as illustrated by intensity profiles that show peaks at the same spatial interval as the ridge spacings (Figure 2, b and e). Optical sectioning by iSIM showed that F-actin accumulates on the sides and at the base of the ridges, but not at the top (Figure 2c). This enrichment of actin near the ridges was observed for all spacings and was reflected in a significant increase in the
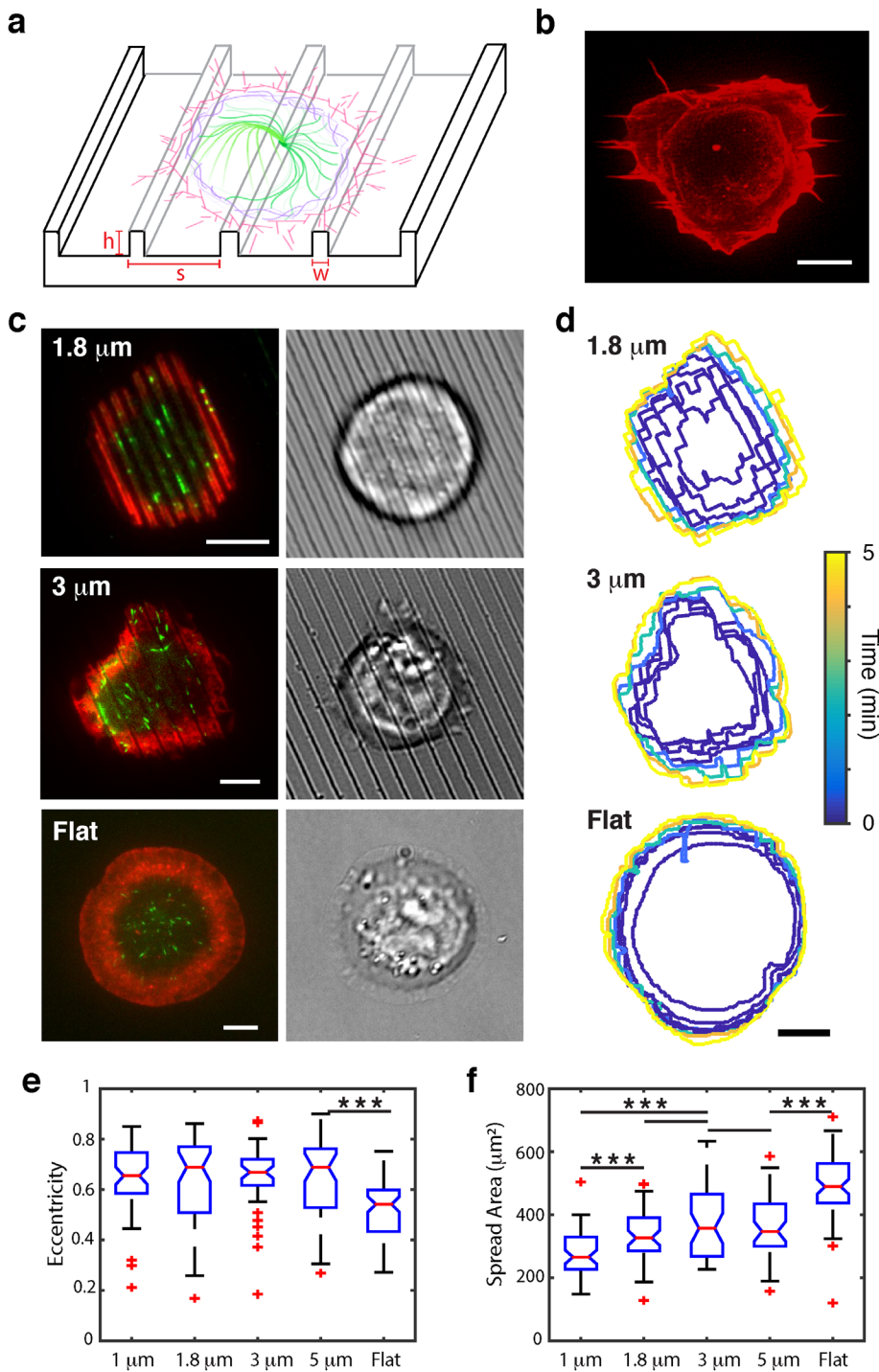
FIGURE 1: Activation-induced spreading of T cells on patterned substrates. (a) Schematic showing the patterned substrates, which are composed of ridges of height *h*, width *w*, and repeat distance *s*. (b) Maximum intensity projection of fluorescence from rhodamine-phalloidin-labeled actin (red) of a fixed Jurkat T cell activated on nanoridges with a 3-µm spacing, imaged with iSIM in 3D. (c) Live T cells spreading on nanopatterned substrates of indicated ridge spacings and a flat surface, imaged with TIRF microscopy. Left panels: composite fluorescence images of cells expressing TagRFP-T-actin (red) and EGFP-EB3 (green). Right panels: bright-field images of the same cells. (d) Cell contours color coded for the time from which imaging started for the indicated spacings and flat surface. (e) Eccentricity of the cell shape as measured from the cell contours of fixed cells at different nanoridge spacings. (f) Spread area of cells fixed after 6 min of activation for different nanoridge spacings. $N = 54$ cells for 1 µm, $N = 49$ for 1.8 µm, $N = 42$ for 3 µm, $N = 45$ for 5 µm, and $N = 70$ for flat. Significance of differences was tested using Kolmogorov-Smirnoff test (***$p < 0.001$, **$p < 0.01$, *$p < 0.05$). All scale bars are 5 µm. For the

peak-to-mean (PtoM) ratio of actin fluorescence intensity (see *Materials and Methods*) for all ridge spacings as compared with on flat regions of the substrates (Figure 2f).

We next investigated whether the accumulation of F-actin near the ridges is concurrent with accumulation of signaling molecules recruited to microclusters. Accumulation of the kinase ZAP-70 (zeta-chain-associated protein kinase-70) to TCR microclusters occurs at the early stages following receptor activation (Samelson *et al.*, 1986) and thus provides a good indicator of the spatiotemporal distribution of signaling molecules. To examine the distribution of ZAP-70 and F-actin simultaneously, YFP-ZAP-70-expressing Jurkat T cells were fixed and stained with rhodamine-phalloidin and imaged using iSIM (Figure 3a and Supplemental Figure S2a). We observed lateral and axial colocalization of actin and ZAP-70 at the bottom and sides of the ridges (Figure 3b and Supplemental Figure S2b). We found that the fluorescence intensity of ZAP-70 was highest at the location of the ridges, matching the distribution of actin (Figure 3c and Supplemental Figure S2c). This colocalization indicates that nanoscale features of the substrate lead to spatial patterning of T cell signaling molecules. We further noted that while ZAP-70 microclusters were nearly uniformly distributed throughout the contact region for cells on flat regions, these microclusters were enriched along the ridges (Supplemental Video S1). To quantify this accumulation across the population, we computed the PtoM ratio of the fluorescence intensity of ZAP-70 microclusters (see *Materials and Methods*). We found that the ridges induced a significant increase in the PtoM ratio for smaller ridge spacings (1.8 µm) compared with larger (3 and 5 µm) spacings and to cells on flat portions of the substrates (Supplemental Figure S2d). To study the influence of topography on signaling further, we fixed cells at 6 min and stained for phosphorylated Zap70 (Tyr 319) (pZap70). Cells on ridges with smaller spacings showed higher accumulation of pZap70 than cells on ridges with larger spacings and flat surfaces, as shown in images of individual cells color coded for intensity (Figure 3d and Supplemental Figure S2e) and summarized in

box plots the red line represents the median, the bottom line represents the lower quartile, the upper line represents the upper quartile, the whiskers show the extent of the rest of the data, and red crosses are the outliers.
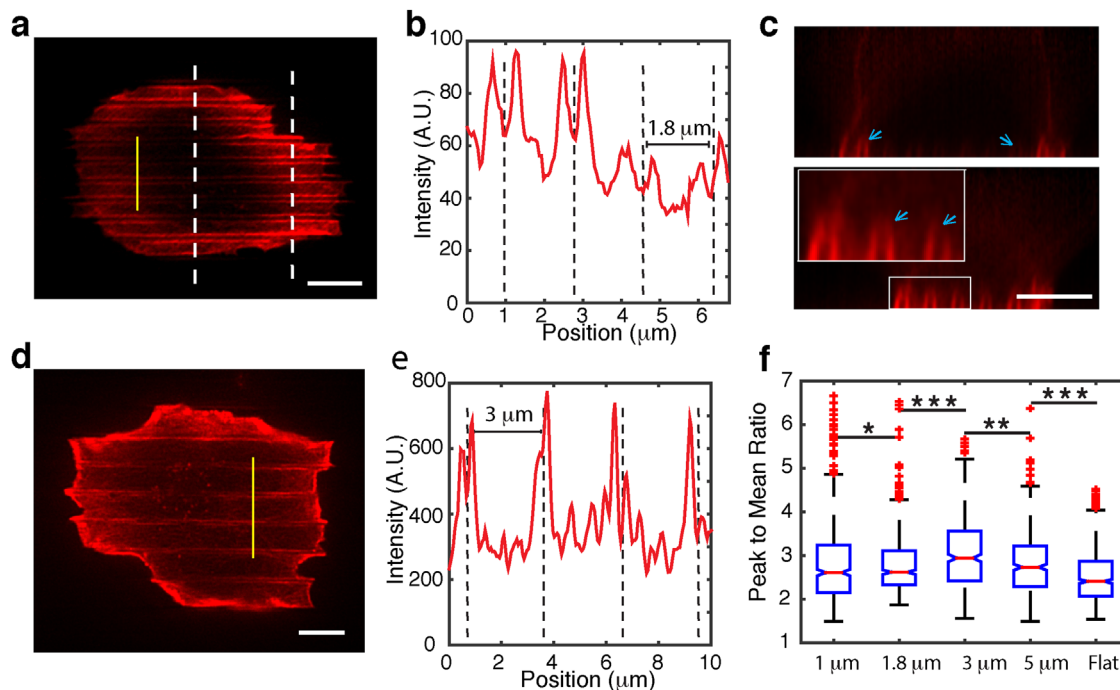
FIGURE 2: Nanotopography alters actin distribution in activated T cells. (a) iSIM image of Jurkat T cells that were activated on ridges with a 1.8-μm spacing and then fixed and stained with rhodamine-phalloidin to label F-actin. (b) Fluorescence intensity of labeled actin plotted along the yellow line shown in (a). The dashed lines indicate the positions of the ridges. (c) The *xz* reslice along the white dashed lines shown in (a); the top panel corresponds to the left dashed line and the bottom panel corresponds to the right dashed line. The arrows indicate the enrichment of actin along the sides of the ridges. (d) iSIM image of a Jurkat T cell activated on ridges with a 3-μm spacing. (e) Fluorescence intensity of labeled actin plotted along the yellow line shown in (d). The dashed lines indicate the positions of the ridges. (f) Ratio of PtoM intensity of F-actin fluorescence for cells on nanoridges with different spacings. The red lines denote the median, the bottom lines denote the lower quartile, the upper lines denote the upper quartile, the whiskers show the extent of the remainder of the data, and the red crosses are the outliers. $N = 54$ cells for 1 μm, $N = 49$ for 1.8 μm, $N = 42$ for 3 μm, $N = 45$ for 5 μm, and $N = 70$ for flat. Kolmogorov-Smirnoff test with ***$p < 0.001$, **$p < 0.01$, *$p < 0.05$. All scale bars are 5 μm.

Figure 3e by the mean fluorescence intensity (MFI) of pZap70. Taken together, these observations suggest that membrane topography plays a key role in the spatial patterning of signaling assemblies.

Nanotopography modulates actin dynamics of T cells during activation

We next investigated the influence of nanotopography on actin dynamics of activated T cells using live-cell TIRF imaging to visualize the interface between the cell and the substrate. T cells are known to exhibit considerable actin remodeling and flows at the cell periphery, with a central region that is largely depleted of actin (Yi *et al.*, 2012; Murugesan *et al.*, 2016) (see Figures 1c and 3a). We observed that for T cells spreading on flat surfaces, actin reorganization and dynamics occurred mostly in the peripheral region of the cells (Figure 4a, upper panels). On the other hand, cells spreading on nanoridges exhibited extensive actin dynamics along the ridges that persisted even after complete spreading (Figure 4, a, bottom panels, b; and Supplemental Video S2). Representative kymographs of cells on flat substrates along radial directions clearly exhibit retrograde actin flows as the cell edge advances (Supplemental Figure S3a). However, for cells on patterned surfaces, the kymographs parallel to the ridges show disorganized retrograde flow. There are clear streaks in actin intensities that indicate that actin waves do not move perpendicularly to the ridges (Supplemental Figure S3b). Thus the presence of nanoscale features alters actin retrograde flow at the IS.

To quantify the effect of topography on the spatial distribution of actin dynamics, the pixelwise temporal coefficient of variation (CV) was calculated using $CV = \sigma/\mu$, where σ and μ are the SD and the mean intensity (Smoligovets *et al.*, 2012; Ketchum *et al.*, 2018), respectively, of the region considered over a 60-s window on spread cells. Figure 4c shows the heatmap of the CV obtained for the same cells shown in Figure 4b, with warmer colors indicating higher actin dynamics. We found that whereas cells on flat substrates showed enhanced dynamics in a thin region around the advancing cell edge, cells on nanoridges with 1.8- and 3-μm spacings exhibited increased actin dynamics throughout the contact zone, particularly along the ridges. These differences are apparent in the cumulative distribution function of pixelwise CVs in Figure 4d, which shows overall larger values for cells on ridges compared with cells on flat surfaces, with the largest values observed on ridges with the narrowest spacing (1.8 μm). These differences were preserved for cells on nonstimulatory PLL-coated substrates (Supplemental Figure S3, c and d).

Previous work has shown that nanopatterned substrates can induce coherent actin flows and directional actin waves (esotaxis) (Driscoll *et al.*, 2014; Sun *et al.*, 2015; Ketchum *et al.*, 2018; Lee *et al.*, 2020). We thus used optical flow, a computer-vision algorithm that can track displacements by calculating the pixelwise gradient of intensities between consecutive frames, to explore whether ridges influence the directionality of actin dynamics (Figure 5a). Optical flow has been used previously to demonstrate the guidance of actin
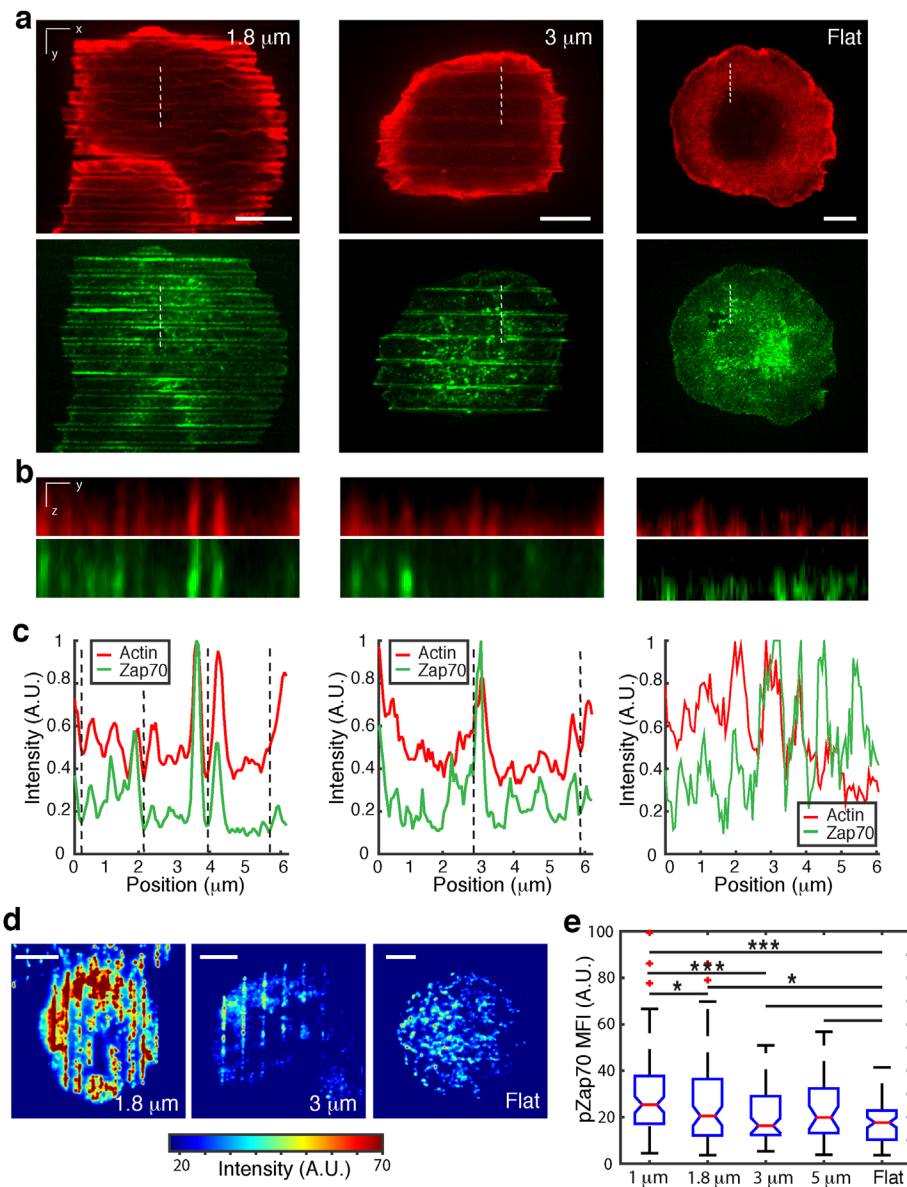
FIGURE 3: Nanotopography modulates ZAP-70 distribution and accumulation (a) iSIM image of YFP-ZAP-70 Jurkat cells fixed and stained with rhodamine-phalloidin after 6 min of activation on nanopatterned surfaces with 1.8-μm (left) and 3-μm (center) spacings, and flat surfaces (right) showing F-actin in red and ZAP-70 in green. (b) The *yz* resliced (representing a 1-μm axial portion of the cell) image along the dashed line in (a) showing the lateral distributions of F-actin and ZAP-70 and their accumulation along the ridges. (c) Fluorescence intensity profile along the dashed lines for F-actin (red) and ZAP-70 (green). (d) TIRF images of pZap70 on cells fixed after 6 min of activation on substrates with nanoridges at the indicated spacings. The images are color coded for intensity. (e) Plots of MFI measured on cells fixed after 6 min of activation and stained for pZap70. The red line represents the median, the bottom line represents the lower quartile, the upper line represents the upper quartile, the whiskers show the extent of the remainder of the data, and the red crosses are the outliers. Kolmogorov-Smirnoff test (***p < 0.001, **p < 0.01, *p < 0.05). Numbers of cells are 85 for 1 μm, 81 for 1.8 μm, 65 for 3 μm, 38 for 5 μm, and 80 for flat. All scale bars are 5 μm.

calculated with respect to a vertical line, and angles were obtained from $\tan^{-1}\frac{v_y}{v_x}$, where v_y and v_x are the *y* and *x* components of the velocity at each pixel, respectively. We found that actin flows were oriented preferentially parallel to the ridges (see insets in Figure 5b, left). This effect was most pronounced for smaller ridge spacings as shown by polar histograms of flow directionality for individual cells (Figure 5c and Supplemental Figure S4a) as well as by the overall probability distribution of actin flow directionality (Figure 5f). In contrast, cells on flat surfaces displayed more isotropic flow of actin in all directions during cell activation (Figures 5, b and c, right panels). Surprisingly, actin flow was clearly guided by ridges even for cells that spread across the patterns (see Supplemental Video S4 and Supplemental Figure S4b). As these cells encountered and spread across a new ridge, actin flowed along the space between ridges and mostly parallel to the ridges, with an unknown constraint driving the cell to continue spreading across the barrier.

For further quantification, we fit the distribution of flow vectors to a von Mises distribution (orange lines in Figure 5c) parametrized by an angle θ, which indicates the mean direction, and 1/κ, which represents the width of the distribution (Lee *et al.*, 2020). We found that κ progressively decreases for larger spacings (Figure 5d), indicating that the distribution becomes wider at increased ridge spacings. Moreover, the mean direction of motion, θ, is strongly aligned with the ridges (Figure 5e). In comparison, the directions of the flow vectors are uniformly distributed on flat substrates. Finally, we calculated the probability distribution of actin directionality for all cells in a 0 to 90° range (Figure 5f). We found that all angles are equally likely for cells on flat surfaces, but that the likelihood of angles near 90° (parallel to the ridges) increases with decreasing pattern spacing. Interestingly, cells on PLL-coated substrates (nonactivated) displayed more disorganized actin flows with less alignment with the ridges (Supplemental Figure S4, c and d) suggesting that the high alignment observed in activated cells depends on the specific actin reorganization/remodeling induced by the CD3 activation signal.

waves in migrating cells induced by nanotopographic features (Lee *et al.*, 2020). Using this method, we obtained vector maps of the actin flow directionality for cells activated on nanoridges with different spacings (Figure 5b and Supplemental Video S3). Images of cells on nanotopographic surfaces were rotated such that the ridges were vertical (90° in the lab frame). Flow directionality was

Nanotopography modulates MT tip orientation and dynamics

Although formation of the IS is characterized by rich actin dynamics, the maturation of the synapse depends upon the polarization and dynamics of the MT cytoskeleton (Martín-Cófreces *et al.*, 2008; Bustos-Morán *et al.*, 2017). MTs regulate retrograde actin flow and
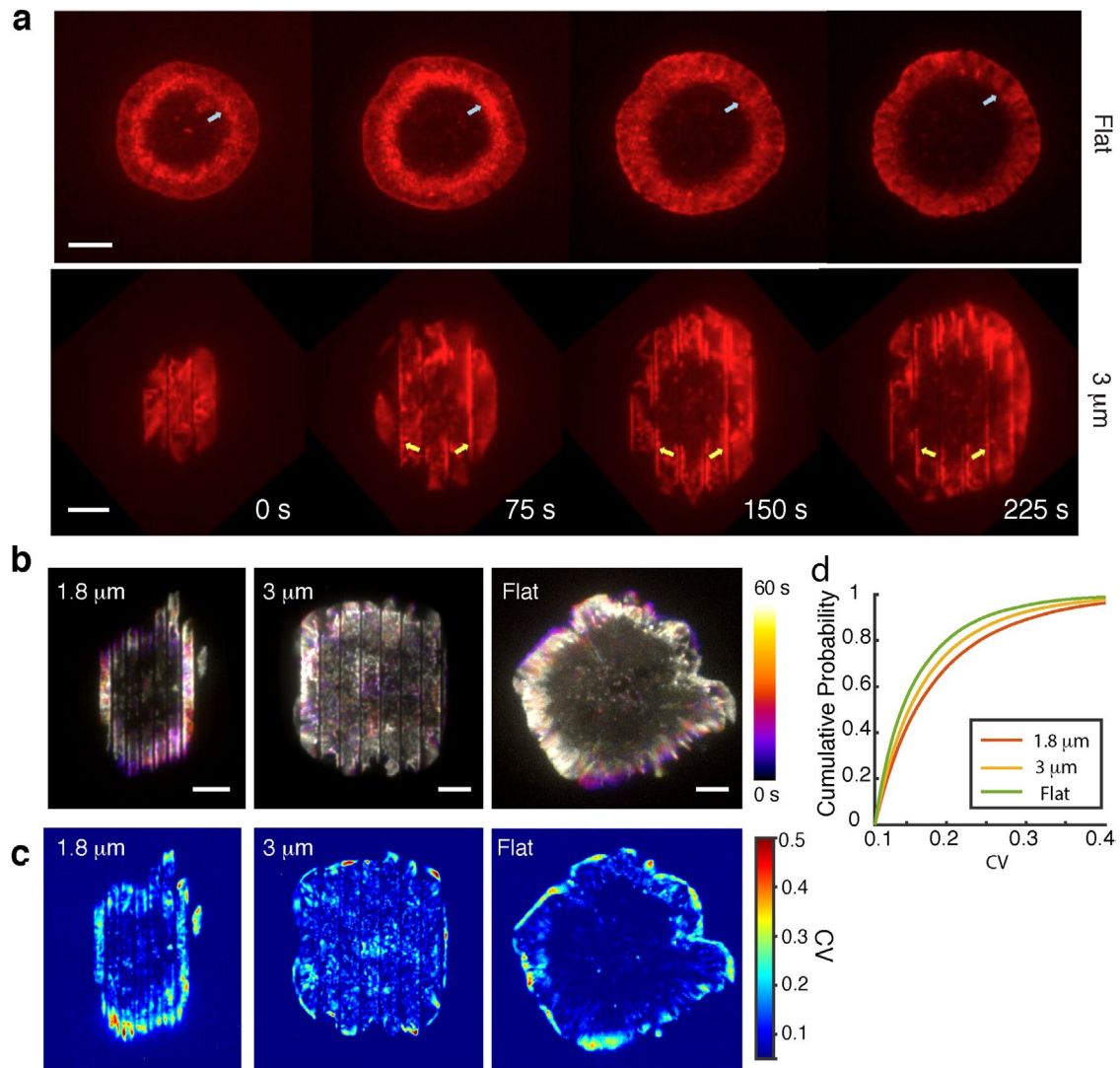
FIGURE 4: Nanotopography modulates actin dynamics of activated T cells. (a) TIRF images of TagRFP-T-actin Jurkat T cells spreading on a flat substrate (top panels) and on a substrate with a 3-µm ridge spacing (bottom panels). The blue arrows indicate actin dynamics at the periphery of the spreading cell. The yellow arrows indicate the persistence of dynamic actin accumulation along ridges as the cell spreads. (b) Color-coded maximum intensity projections of actin fluorescence over time for a cell activated on a substrate with ridges spaced by 1.8 µm (left), a cell on a substrate with ridges spaced by 3 µm (center), and a cell on a flat substrate (right). The white color regions indicate the superposition of maximum actin fluorescence intensity at different times. (c) Color-coded maps of the coefficient of variation (CV) of the intensity per pixel for the cells shown in (b). (d) CDF plots of the pixelwise CV calculated for cells activated on substrates with 1.8-µm and 3-µm ridge spacings and flat substrates. To eliminate the effect of cell background fluctuations, only CV values larger than 0.1 were considered for the plot. $N = 15$ for 1.8 µm, $N = 12$ for 3 µm, and $N = 10$ for flat. The scale bars are 5 µm for all images.

actomyosin force generation through suppression of Rho GTPase activation (Hui and Upadhyaya, 2017), and the distinct actin network architectures in T cells in turn modulate MT deformation and growth dynamics (Rey-Suarez *et al.*, 2021). Given the important role of MTs during T cell activation and the limited understanding of how the nanotopography of the T cell/APC interface affects MT dynamics, we examined how nanoridges modulate MT growth and spatial organization. We fixed cells at 6 min after activation, immunostained for beta-tubulin, and imaged using iSIM. We observed that the centrosome repositioned to the contact plane regardless of whether cells had been activated on patterned or flat portions of the substrate (Figure 6a and Supplemental Figure S5, a and c). However, MT filaments on nanoridges appeared to align with the ridges (examples shown with blue arrowheads), indicating that nanoridges influence MT organization at the contact zone. We next used TIRF to image MT growth dynamics in cells expressing TagRFP-T-actin and EGFP-EB3 (Figure 6b and Supplemental Video S5). EB3 is a plus-end MT-binding protein that is used regularly as a marker to measure MT growth rates (Gierke *et al.*, 2010; Matov *et al.*, 2010). MT dynamics were measured by detecting and tracking EGFP-EB3 using the MATLAB-based tracking software *uTrack* (Jaqaman *et al.*, 2008). Bright-field images were used for ridge detection, where the angle of the ridge was defined relative to the *x*- and *y*-axis of the frame (see *Materials and Methods*). Tracked displacements of MT plus ends showed that the trajectories became increasingly aligned with ridges for smaller ridge spacing (Figure 6c).
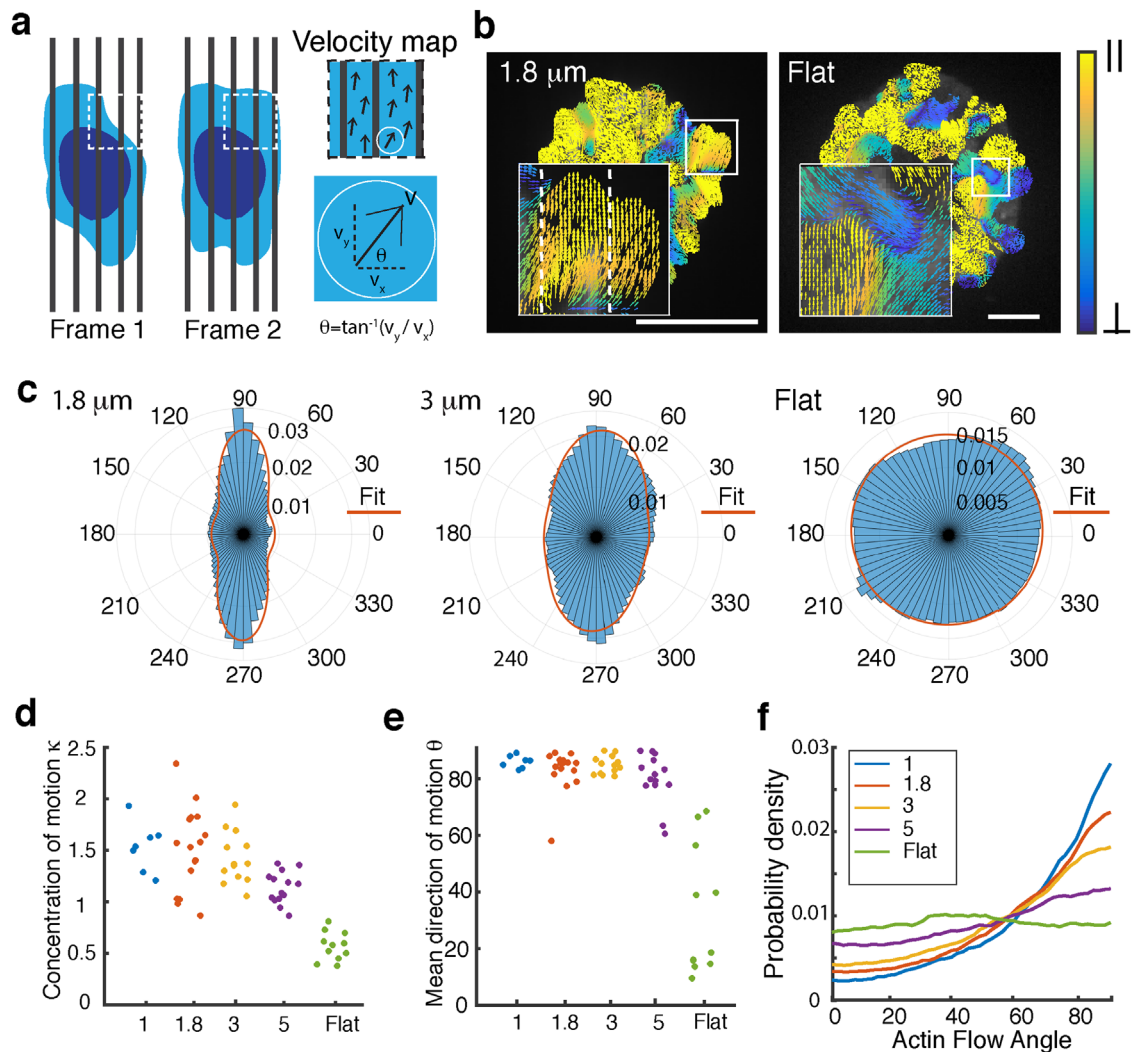
FIGURE 5: Actin flow directionality is guided by nanoridges. (a) Schematic showing how actin directionality is calculated from a vector map of the intensity gradient between consecutive frames using optical-flow analysis. (b) Actin flow vector maps obtained using optical-flow analysis on TIRF movies of RFP-actin Jurkat cells while spreading on nanotopographic substrates. Warmer colors correspond to flow aligned with the ridges, and cooler colors correspond to flow perpendicular to the ridge orientation. The scale bars are 5 μm. (c) Representative polar histograms of actin flow directionality for single cells obtained from optical-flow analysis. An angle of 90° is along the ridges. (d) Plot of the concentration of motion of the actin directionality (parameter κ from the von Mises fit) vs ridge spacing. (e) The mean direction of motion (θ) plotted in a 0 to 90° range for different ridge spacings. In panels (d) and (e), each dot represents a cell. (f) Probability distribution plots of the actin flow directionality for cells on substrates with different ridge spacings on a 0–90° range. Flat $N = 11$ cells, 5 μm $N = 14$, 3 μm $N = 13$, 1.8 μm $N = 16$, and 1 μm $N = 8$.

To quantify the directionality of MT growth, we defined the instantaneous angle as the angle between the direction of interframe displacement vector (the displacement between two consecutive frames) and the direction of the nanoridges. The instantaneous angle was defined to be the smallest angle between the vector and the ridges, taking on a value between 0 and 90°. For cells on flat surfaces, a line at an arbitrary angle relative to the vertical axis was chosen as a reference. The instantaneous angle distributions show that EB3 trajectories align with ridges on nanotopographic substrates (Figure 6, d and e). This alignment was most notable on ridges with the smallest spacing, which showed the least angular deviation from the ridges. In contrast, for EB3 trajectories of cells on flat portions of the substrates, instantaneous angles from 0 to 90° were equally likely (Figure 6e). Furthermore, we found that the alignment of EB3 along ridges was sustained over the course of the entire trajectory, as measured by the alignment value (Figure 6f; see *Materials and Methods* for definition). We again found that the highest alignment occurred for the smallest nanoridge spacings (1 and 1.8 μm) (Figure 6f). We defined the alignment order parameter (Figure 6g) as the alignment between the EB3 tracks of a cell. This quantity is a global measure of oriented MT growth. We found that the alignment between EB3 tracks was greater on ridges with smaller spacings. We next quantified the instantaneous speed of MT growth from the interframe displacements of EB3 tracks calculated over 3-s time intervals between images. We found that the growth velocities were highest for 1.8-μm ridge spacing, suggesting the existence of an optimum spacing for MT growth (Figure 6, h and i). Overall, these results show that antigen-presenting surface nanotopography influences MT distribution and dynamics. However, topography
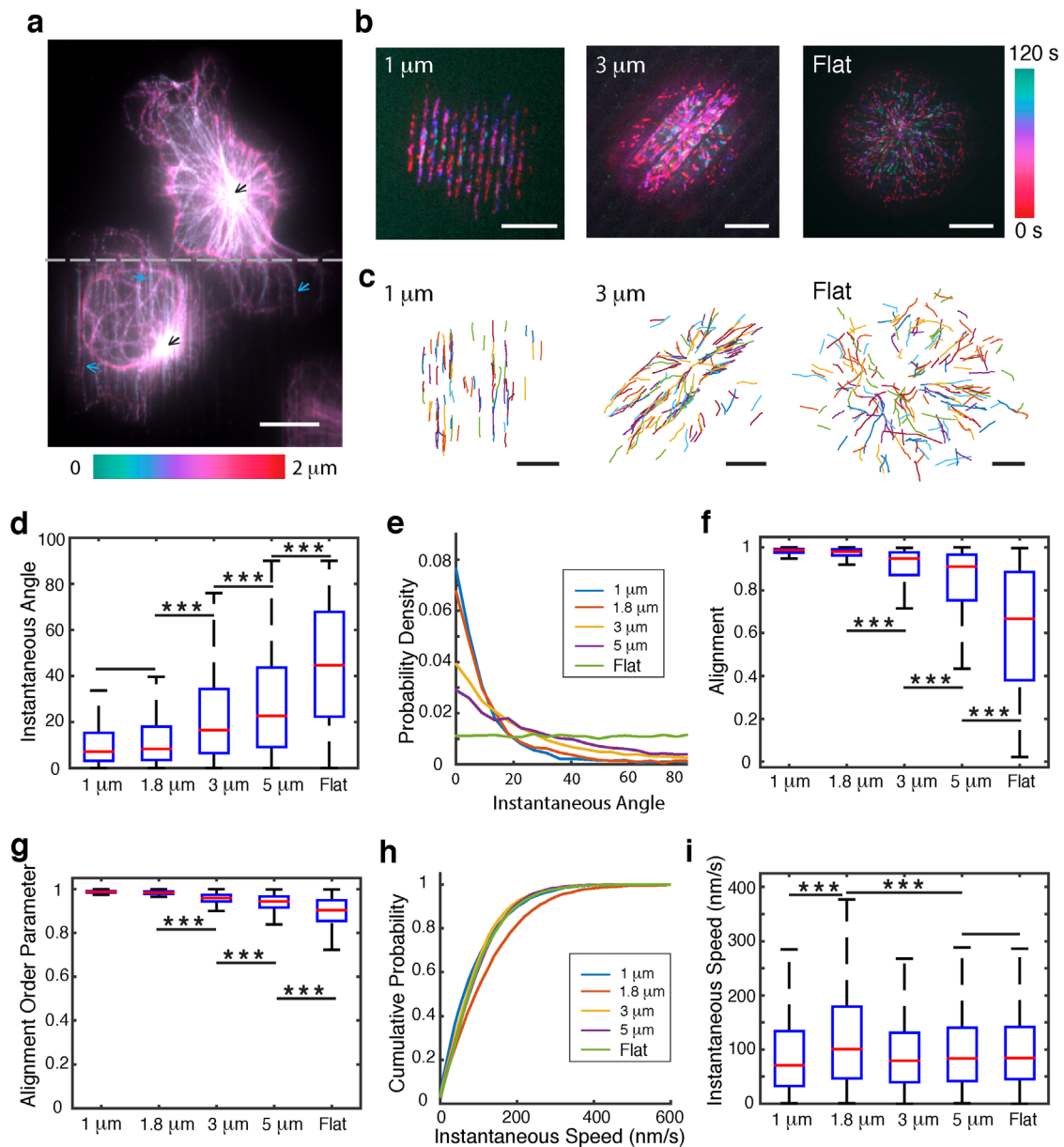
FIGURE 6: Nanotopography modulates MT tip orientation and dynamics. (a) Maximum intensity projection color coded for height of Jurkat T cells fixed at 6 min after activation, immunostained for beta-tubulin, and imaged with iSIM. The dashed gray line indicates the separation between the flat (top) and the patterned (bottom) sections of the same substrate. The blue arrows point to MT filaments aligned between ridges and the black arrows point to the centrosome. (b) Maximum intensity projection color coded for time of live EGFP-EB3 Jurkat T cells during activation. (c) Compilation of EB3 tracks for the cells shown in (b). (d) Plots of instantaneous angle, defined as the smallest angle between an interframe displacement and the ridge, for the ridge spacings considered. For the cells on flat substrates an arbitrary line was used to calculate the angles. Scale bars are 3 μm. (e) Probability distribution of the instantaneous angle for cells on substrates with the indicated ridge spacings and flat substrates. (f) Comparison of the alignment value of EB3 tracks on different nanoridge spacings. (g) Comparison of the alignment order parameter of EB3 tracks on substrates with the indicated ridge spacings. (h) Cumulative probability distribution of instantaneous speeds of EB3 movement for different nanoridge spacings. (i) Box plots of instantaneous speed of EB3. The scale bar for all panels is 5 μm. For the box plots the red line represents the median, the bottom line represents the lower quartile, the upper line represents the upper quartile, the whiskers show the extent of the remainder of the data, and the red crosses are the outliers. Significance of difference was tested using the Kolmogorov-Smirnoff test (***$p < 0.001$, **$p < 0.01$, *$p < 0.05$). Number of cells for flat $N = 11$, for 5 μm $N = 14$, for 3 μm $N = 13$, for 1.8 μm $N = 16$, 1 μm $N = 8$.

alone is not sufficient to induce centrosome repositioning without the activation signal (Supplemental Figure S5, b and d) and MT tip trajectories appear to be less aligned on ridges (Supplemental Video S6).

DISCUSSION

T cells navigate complex microenvironments with varied physical properties, including mechanical stiffness, fluidity, and topography. How TCR activation integrates these mechanical signals with antigen

and cytokine induced biochemical signaling is a subject of extensive investigation. High-resolution imaging of planar interfaces for T cell activation has shown that the organization and dynamics of the actin cytoskeleton are essential for sensing the mechanical properties of antigen-presenting surfaces. Antigen-presenting cells possess complex surfaces with convoluted topographies, including long extensions, dendrites, membrane ruffles, and invaginations (Felts *et al.*, 2010; Saino *et al.*, 2011) with radii of curvature ranging from 100 to 300 nm (Szakal *et al.*, 1985; Felts *et al.*, 2010). Such topographic features lead to the accumulation of curvature-sensing proteins at the cell membrane, and the subsequent induction of actin polymerization via N-WASP and other actin nucleating proteins (Galic *et al.*, 2012). Taking advantage of substrate features with dimensions that mimic those encountered by T cells in vivo, we performed a systematic study of the effect of nanotopography on cytoskeletal dynamics and TCR signaling. We found that nanopatterned surfaces influence cell morphology, spatial organization of actin cytoskeleton, and signaling microclusters, as well as actin and MT dynamics.

The IS is characterized by actin enrichment at the periphery, generating an actin ring (Hammer *et al.*, 2018). The presence of this peripheral enrichment is also observed for cells on patterned surfaces. However, in contrast with the peripheral actin ring that is characteristic of planar substrates, we found that F-actin accumulates along the bottom surface on nanoridges. Studies have shown that F-actin accumulates as distinct puncta on nanopillars that are not connected to stress fibers or adjacent to focal adhesion complexes (Biggs *et al.*, 2010; Lou *et al.*, 2018). Another study using 1- to 2-micron-long nanobars showed that F-actin accumulates at the nanobar ends, with little accumulation along the flat sidewalls (Zhao *et al.*, 2017). In contrast, Ketchum *et al.* found that nanoridged surfaces, similar to those used here, induce global actin-intensity oscillations in B cells, in addition to ridge-adjacent increases in actin density (Ketchum *et al.*, 2018). Collectively, these studies imply a role for membrane curvature in inducing actin accumulation (Galic *et al.*, 2012), but the connection between actin polymerization and local membrane curvature is still poorly understood.

During T cell activation, the stimulation of the TCR leads to the formation of microclusters that recruit a number of signaling proteins that form the basis of early T cell signaling. We found increased accumulation of the signaling kinase ZAP-70, as well as its activated form (pZAP-70), in cells activated on ridges with small spacings compared with cells on larger spacings and flat surfaces, suggesting that nanotopography enhances microcluster formation and signaling. Similar nanotopographically induced up-regulation of BCR (B cell receptor) signaling clusters have been described for B cells activated on nanopatterned substrates (Ketchum *et al.*, 2018). The influence of nanotopography on intracellular protein clustering has been most extensively explored in the context of integrin-mediated focal adhesions in adherent cells (Biggs *et al.*, 2010). This study suggested that integrin clusters are largely confined to interfeature regions, which limit their sizes and signaling downstream via focal adhesion formation and activation of various kinases as well as the forces exerted by the actin cytoskeleton. Finally, (Mossman *et al.*, 2005) have shown that physical barriers (~10 nm height, 100 nm width, 2 to 5 μm spacing) on supported lipid bilayers can disrupt the transport of TCR microclusters via actin retrograde flow (Mossman *et al.*, 2005). The presence of these barriers induces microcluster accumulation, transient actin enrichments, and actin-flow-speed reduction (Yu *et al.*, 2010; Smoligovets *et al.*, 2012). Together, these observations suggest a general principle for receptor-mediated protein clustering. There appears to be positive feedback between actin and signaling, wherein higher actin polymerization, potentially induced by local regions of high curvature, leads to receptor clustering, which in turn enhances actin polymerization due to enhanced recruitment of actin regulators downstream of the signaling clusters.

Nanopatterns not only affect the distribution of actin but also its dynamics. Evaluation of actin dynamics through variations in fluorescence intensity showed that there are larger actin intensity fluctuations for cells on nanotopographic surfaces as compared with cells on flat surfaces. These higher actin dynamics are likely related to the greater accumulation of ZAP-70 near the ridges and suggest a positive feedback between actin and signaling microclusters. Despite the difference in actin dynamics, the spreading rates were the same for cells on all nanoridge spacings. We also observed that the ridges guide the actin flow and that this effect is more pronounced in narrower spacings. Actin-rich lamellipodial protrusions and integrin-mediated adhesions aligned with topographical features are essential for T cell migration in the absence of confinement (Kwon *et al.*, 2012, 2013). Cell migration guided by nano/microtopography, known as microthigmotaxis (Sun *et al.*, 2015), has been described for a variety of cell types and originates from the unidirectional bias of actin polymerization waves that favors cell movement along nanoscale features (esotaxis) (Driscoll *et al.*, 2014; Sun *et al.*, 2015; Lee *et al.*, 2020). Although such actin flows in Jurkat cells are primarily due to actin polymerization, we cannot rule out a contribution for myosin contractility in shaping the actin network structure and its alignment to topographic features.

We also observed that the presence of nanotopography influences the distribution and dynamics of the MT cytoskeleton. The alignment of MTs with nanostructures has been previously described for different cell types seeded on nanopatterned substrates (Gerecht *et al.*, 2007; Lee *et al.*, 2016; Sun *et al.*, 2018). For migrating cancer cells, the MT network produces a structural scaffold that regulates steric interactions during contact guidance with nanotopographic cues (Tabdanov *et al.*, 2018). Although MT alignment by nanotopography has been reported, the influence of nanotopography on MT dynamics is not well understood. We found that the growth of MTs was guided by the presence of the ridges, which possibly explains the alignment of the filaments that we and others have reported (Lee *et al.*, 2016; Tabdanov *et al.*, 2018). MT growth alignment was similar for spacings smaller than 1.8 μm, suggesting a limit to the filaments' capability to align with nanostructures. Interestingly, MT growth speed was the same on flat surfaces and for all ridge spacings studied here except 1.8 μm, on which the growth speed was higher. Growing MTs can be captured and guided along actin bundles through the interaction of actin/MT crosslinkers and MT-end-binding proteins (López *et al.*, 2014). This particular spacing may enable the generation of specific actin structures, which may act synergistically with steric barriers imposed by the ridges to regulate MT growth and stability. Similar to observations on migrating cancer cells (Tabdanov *et al.*, 2018), we anticipate that steric effects, which largely dominate in ridges with smaller spacing, induce formation of formin-mediated actin bundles that stabilize and enhance MT growth along the ridges. However, the ridges preclude formation of formin-induced actomyosin arcs that are prominent in the IS (Murugesan *et al.*, 2016), which serve to guide nonradial MT growth. In contrast, on substrates with wider ridge spacing, flows within branched F-actin networks impose steric effects and forces on MTs, slowing their growth as well inducing large-scale deformations. The results presented here further our understanding of how subcellular topography modulates actin and MT dynamics in the context of the early stages of IS formation.

We finally note that the steric effects of topography are still operant without activation of TCR/CD3 signaling. The adhesive effects of

PLL alone are sufficient to induce spreading of the cells and enhance actin dynamics near the ridges. In part, these might arise due to the accumulation of curvature-sensitive actin nucleation regulators (Galic et al., 2012). The further activation of actin dynamics by TCR/CD3 signaling augments the effect induced by topography, which manifests in the changes in signaling and cytoskeletal dynamics that we observe.

Our results suggest that the topographically complex surfaces encountered by T cells in vivo are likely to affect both morphology and cytoskeletal dynamics, with consequent effects on TCR organization and signaling. Other types of nanotopographic features, such as nanoposts, nanopits, and fibers, which can be fabricated by the optical techniques used here, may shed further light on how specific nanotopographic features modulate T cell signaling. Moreover, recent advances in nanopatterning (Tabdanov et al., 2018; Bhingardive et al., 2021; Mordechay et al., 2021) enable fabrication of compliant substrates with nanoscale features. Such substrates will facilitate future explorations of the interaction between mechanical rigidity and topography of activating substrates in T cell activation. A recent study of CD8 positive T cells activated on micron-scale patterned surfaces (Fella et al., 2020) noted a segregation of Arp2/3 regulators at different regions of surface features—with WAVE-2 being enriched at the cell periphery and WASP preferentially accumulating at the edges of microposts. How these distinct Arp2/3 regulators segregate and organize actin networks on nanoridges remains an open question. In contrast with Jurkat cells, primary T cells are known to have more dynamic edges and that the actin flow velocities are myosin dependent. It is possible that nanotopography would induce global actomyosin oscillations in primary T cells as we have observed in primary naïve B cells (Ketchum et al., 2018). Finally, investigations with inhibitors of actin regulators (Arp2/3 and formins) as well as perturbations of MT dynamics and myosin contractility will help parse out the differential contributions of these cytoskeletal systems to topography sensing and signaling.

Taken together, these studies point to the importance of physical characteristics of ligand presentation, including ligand mobility, substrate stiffness, antigen density, and nanotopography, in T cell activation and the adaptive immune response. This work could aid further advances in the development of bioengineering strategies for antigen-presenting substrates for the development of effective immunological therapies and vaccines.

MATERIALS AND METHODS
Cell culture
Wild-type (WT), YFP-ZAP-70, and EGFP-EB3 + TagRFP-T-Actin E6-1 Jurkat T cells were cultured in RPMI 1640 medium supplemented with 10% fetal bovine serum (FBS) and 1% Penn-Strep antibiotics and passaged 3 d per week. Experiments were typically performed the day after the cells were passaged. For experiments with GFP-centrin cells, transient transfections were performed using the Neon (Thermo Fisher Scientific) electroporation system 2 d before the experiment. The protocol was as follows: 2×10^5 cells were resuspended in 10 µl of R-buffer with 0.5–2 µg of the plasmid. The cells were exposed to three pulses of amplitude 1325 V and duration 10 ms in the electroporator. Cells were then transferred to 500 µl of RPMI 1640 supplemented with 10% FBS and kept in the incubator at 37°C. Before imaging, 1 ml of cultured cells was centrifuged at $250 \times g$ for 5 min. The supernatant was removed and the cells were resuspended in L-15 imaging medium. pEGFP Centrin2 (Nigg UK185) was a gift from Erich Nigg (Addgene plasmid# 41147).

Microscopy
TIRF imaging was performed on an inverted microscope (Nikon Ti2000 PFS) equipped with a 1.49 numerical aperture, 60× objective, and a scientific CMOS camera (Zyla 4.2, Andor-Oxford). Imaging protocols were implemented using the software Elements from Nikon, and images were cropped using Fiji before further analysis using MATLAB scripts. Time-lapse movies were taken with a 3-s time interval for 10 min from the start of cell spreading. For each time-lapse movie, a bright-field image was taken to register the location of the ridges. Imaging of fixed Jurkat T cells was performed using iSIM, with a 1.42 numerical aperture, 60× objective (Olympus), 488- and 546-nm lasers for excitation, and a scientific CMOS camera (Edge, PCO-Tech). For 3D imaging, the exposure time was 120 ms per slice and the spacing between Z slices was 200 nm. The iSIM images obtained were postprocessed with background subtraction and deconvolution. The final lateral resolution for deconvolved images was between 140 and 150 nm. The Richardson–Lucy algorithm was used for deconvolution and run for 10 iterations. The point spread function (PSF) used was simulated by a Gaussian function based on parameters obtained from measurement, i.e., the full width at half maximum (FWHM) of the PSF used is the same as the FWHM measured. Confocal imaging of fixed GFP-centrin cells was performed on the same TIRF microscope described above with a W1 confocal unit and a silicon immersion 100× lens with 1.35 numerical aperture coupled with a Prime BSI CMOS camera (pixel size of 65 nm). Confocal stacks were taken using 300 nm spacing between slices with a 16.5 µm total range (55 slices).

Immunofluorescence
WT, YFP-ZAP-70, or GFP-centrin Jurkat T cells were fixed 6 min after being added to the substrates using 4% PFA (Electron Microscopy Sciences). Cells were then permeabilized using 0.15% TritonX and the samples were blocked using 0.3 M glycine and bovine serum albumin. For MT staining, beta tubulin antibody (Thermofisher Cat#PA5-16863) was used as primary antibody and Alexa Fluor-488 (Invitrogen, Cat# A10235) was used for secondary antibody. For pZap70 staining phospho-Zap70 Tyr319 (Cell Signaling Cat# 2701) primary antibody was used. After labeling of MTs or pZap70, F-actin was stained using rhodamine phalloidin (Cytoskeleton, Cat#PHDR1).

Substrate preparation
The fabrication, functionalization, molding, and replication of the nanotopographic patterns have been described in detail (Sun et al., 2015, 2018). The original patterned structures were fabricated using a technique we refer to as MAP (Driscoll et al., 2014; Ketchum et al., 2018). A photopolymerizable resin was prepared from acrylate-based monomers (Sartomer; SR368 and SR499, in a 1:1 ratio by mass), as well as a photoinitiator (Lucirin TPO-L) comprising 2% of the total mass. After sandwiching a drop of this resin between glass slides, the material was exposed to a pulsed laser (Coherent Mira 900-F) passed through a high-numerical-aperture objective (Zeiss alpha-Plan Fluar 100×; numerical aperture 1.45). The laser was tuned to 800 nm to ensure that excitation of the photoinitiator occurred by absorption of multiple photons, allowing for the 3D control of pattern features. A LabVIEW (National Instruments) program was used to control a motorized shutter and piezo stage to dictate where laser exposure occurred within the material. Molds of the original patterns were made from polydimethylsiloxane (PDMS). First, a layer of hard-PDMS was spin-coated onto the chemically functionalized original (40 s, 1000 rpm). This film was allowed to sit at room temperature for 2 h and then was heated for 1 h at 55 to 60°C. Sylgard 184 (Dow Corning; 1:10 mass ratio of elastomer base:curing agent;

4–5 g) was then poured onto the *h*-PDMS film. The mold was formed after heating at 55 to 60°C for 70 min. Replicas of the original patterns were produced by sandwiching a drop of the acrylate resin between an acrylated glass coverslip and the PDMS mold and exposing to UV light (Blak-Ray; B-100AP; 100 W; 365 nm) for 3 min each. The replicas were soaked in ethanol (at least 12 h) and baked at 110°C for 1 h prior to use.

To activate cells, the nanopatterned substrates were incubated in PLL at 0.01% W/V (Sigma Aldrich, St. Louis, MO) for 10 min. PLL was aspirated and the slide was left to dry for 1 h at 37°C. T cell activating antibody coating is performed by incubating the slides in a 10 µg/ml solution of anti-CD3 antibody (Hit-3a, eBiosciences, San Diego, CA) for 2 h at 37°C or overnight at 4°C. Excess anti-CD3 was removed by washing with L-15 imaging media right before the experiment.

Data analysis

For image analysis all cell images were cropped using Fiji and then postprocessed and analyzed using MATLAB (MathWorks, Natick, MA) custom scripts. To obtain the cell contours, pixel values below 500 (camera readout noise) were set to zero and the MATLAB function *imbinarize* was applied over the image. To refine the mask further, the MATLAB functions *bwareaopen* and *imfill* were used to remove smaller detected objects and to fill holes inside the cell, respectively. The eccentricity was calculated using the "Eccentricity" property from the *regionprops* function in MATLAB, defined as that of an ellipse with the same second moment as that of the cell contour at maximum spread area, and was calculated from $e = \frac{c}{a}$ where *c* is the is the distance between the center of the ellipse and the focus and *a* is the semimajor axis (Supplemental Figure S1c). For PtoM analysis of actin distributions, 10 lines at 0.5-µm intervals were drawn in the cell perpendicular to the ridges. The intensity distribution along the lines was determined, and the PtoM intensity was measured. For PtoM analysis of ZAP-70 fluorescence intensity, images of live YFP-ZAP-70 cells were selected at the point of maximum spread area. The ZAP-70 clusters were detected after image segmentation, after which 20 clusters per cell were selected randomly and the ratio of fluorescence intensity of the cluster to the mean intensity of the cell was calculated. For centrosome position calculation, confocal stacks of single GFP-centrin cells stained with rhodamine phalloidin were selected. The confocal slice for which the actin channel had the highest MFI was used to define the synapse (cell-glass contact plane). Then the slice with the highest MFI in the centrin channel was selected as the centrosome position slice. The synapse to centrosome distance was determined from the product of the slice spacing distance (0.3 µm) and the number of confocal slices between the synapse and the centrosome position slice.

EB3 tracking and analysis

EB3 speeds were analyzed using the MATLAB-based routine U-track (Jaqaman *et al.*, 2008), which links particles between consecutive frames using a global combinatorial optimization strategy to identify the most likely set of trajectories in a movie. We used a search radius range of 2 to 8 pixels for frame-to-frame linking. To eliminate tracking errors, we considered only trajectories with more than three interframe displacements (i.e., displacements between two consecutive frames). To evaluate the alignment of EB3 tracks with the ridges, only trajectories with a total displacement larger than 1 micrometer were considered. To identify the ridge orientation, a Hough transform was computed over a binary version of the bright-field image, transforming the image into a parameter space in which the highest intensity pixel corresponds to the most linear object, allowing for the identification of the ridges and the angle between the ridge and the *x*- and *y*-axes of the frame. The alignment value measures the alignment of EB3 tracks with the ridges and is defined by the average of cosines of the instantaneous angles between EB3 tracks and the detected ridge for each cell:

$$\text{Alignment} = \frac{\sum length(EB3\ trajectory) \times \cos\alpha}{\sum length(EB3\ trajectory)} \tag{1}$$

where α is the smallest angle between an EB3 track and the nanoridges, i.e., α is constrained to be between 0 and 90°. We then calculated the alignment order parameter, a measure of the alignment among EB3 tracks themselves.

$$\text{Alignment } O.P. = \frac{\sum length(EB3\ trajectory) \times \cos(\beta - \gamma)}{\sum length(EB3\ trajectory)} \tag{2}$$

Here the angle, β, between EB3 tracks and nanoridges is weighted by the *average* instantaneous angle, γ, between EB3 tracks and nanoridges *for an entire spacing data set*. For the alignment and alignment order parameter, the angle distribution is weighted by the length of each track, so that the angle generated from a small displacement will have less weight than that of a large displacement.

Optical-flow analysis

To measure the directionality of actin flows, we used an optical-flow algorithm based on the Lucas-Kanade method (Lucas and Kanade, 1981). The output from this analysis contains the *x* and *y* components of the velocity, which enables the generation of vector maps that include the directionality of the intensity flow. A mask based in the cell contour and the reliability matrix values was used to remove vectors resulting from noise. The lower reliability threshold used corresponded to 0.005 times the maximum reliability value based on each cell reliability values distribution.

Statistical methods

All statistical tests were performed using the Kolmogorov-Smirnoff test (Massey, 1951) for two distributions using the function kstest2 from MATLAB.

Data and software availability

The image analysis code and all imaging data are available upon request.

REFERENCES

Babich A, Li S, O'Connor RS, Milone MC, Freedman BD, Burkhardt JK (2012). F-actin polymerization and retrograde flow drive sustained PLCγ1 signaling during T cell activation. J Cell Biol 197, 775–787.

Bashour KT, Gondarenko A, Chen H, Shen K, Liu X, Huse M, Hone JC, Kam LC (2014). CD28 and CD3 have complementary roles in T-cell traction forces. Proc Natl Acad Sci USA 111, 2241 LP–2246.

Bhingardive V, Kossover A, Iraqi M, Khand B, Le Saux G, Porgador A, Schvartzman M (2021). Antibody-functionalized nanowires: a tuner for the activation of T cells. Nano Lett 21, 4241–4248.

Biggs MJP, Richards RG, Dalby MJ (2010). Nanotopographical modification: a regulator of cellular function through focal adhesions. Nanomedicine Nanotechnology, Biol Med 6, 619–633.

Bustos-Morán E, Blas-Rus N, Martin-Cófreces NB, Sánchez-Madrid F (2017). Microtubule-associated protein-4 controls nanovesicle dynamics and T cell activation. J Cell Sci 130, 1217 LP–1223.

Cai E, Marchuk K, Beemiller P, Beppler C, Rubashkin MG, Weaver VM, Gérard A, Liu T-L, Chen B-C, Betzig E, et al. (2017). Visualizing dynamic microvillar search and stabilization during ligand detection by T cells. Science (80-) 356, eaal3118.

Driscoll MK, Sun X, Guven C, Fourkas JT, Losert W (2014). Cellular contact guidance through dynamic sensing of nanotopography. ACS Nano 8, 3546–3555.

Fella T, Diana T, Weiyang J, Vitaly B, Hisham B, Ariella K, C. KL, V. AK, Morgan H (2020). Centrioles control the capacity, but not the specificity, of cytotoxic T cell killing. Proc Natl Acad Sci USA 117, 4310–4319.

Felts RL, Narayan K, Estes JD, Shi D, Trubey CM, Fu J, Hartnell LM, Ruthel GT, Schneider DK, Nagashima K, et al. (2010). 3D visualization of HIV transfer at the virological synapse between dendritic cells and T cells. Proc Natl Acad Sci USA 107, 13336 LP–13341.

Galic M, Jeong S, Tsai F-C, Joubert L-M, Wu YI, Hahn KM, Cui Y, Meyer T (2012). External push and internal pull forces recruit curvature-sensing N-BAR domain proteins to the plasma membrane. Nat Cell Biol 14, 874–881.

Gerecht S, Bettinger CJ, Zhang Z, Borenstein JT, Vunjak-Novakovic G, Langer R (2007). The effect of actin disrupting agents on contact guidance of human embryonic stem cells. Biomaterials 28, 4068–4077.

Gierke S, Kumar P, Wittmann T (2010). Analysis of microtubule polymerization dynamics in live cells. Methods Cell Biol 97, 15–33.

Hammer JA, Wang JC, Saeed M, Pedrosa AT (2018). Origin, organization, dynamics, and function of actin and actomyosin networks at the T cell immunological synapse. Annu Rev Immunol 37, 201–224.

Hong J, Murugesan S, Betzig E, Hammer JA (2017). Contractile actomyosin arcs promote the activation of primary mouse T cells in a ligand-dependent manner. PLoS One 12, e0183174–e0183174.

Hsu C-J, Hsieh W-T, Waldman A, Clarke F, Huseby ES, Burkhardt JK, Baumgart T (2012). Ligand mobility modulates immunological synapse formation and T cell activation. PLoS One 7, e32398.

Hui KL, Balagopalan L, Samelson LE, Upadhyaya A (2014). Cytoskeletal forces during signaling activation in Jurkat T-cells. Mol Biol Cell 26, 685–695.

Hui KL, Upadhyaya A (2017). Dynamic microtubules regulate cellular contractility during T-cell activation. Proc Natl Acad Sci USA 114, E4175–E4183.

Huppa JB, Davis MM (2003). T-cell-antigen recognition and the immunological synapse. Nat Rev Immunol 3, 973–983.

Huse M, Le Floc'h A, Liu X (2013). From lipid second messengers to molecular motors: microtubule-organizing center reorientation in T cells. Immunol Rev 256, 95–106.

Jankowska KI, Williamson EK, Roy NH, Blumenthal D, Chandra V, Baumgart T, Burkhardt JK (2018). Integrins modulate T cell receptor signaling by constraining actin flow at the immunological synapse. Front Immunol 9, 25.

Jaqaman K, Loerke D, Mettlen M, Kuwata H, Grinstein S, Schmid SL, Danuser G (2008). Robust single-particle tracking in live-cell time-lapse sequences. Nat Methods 5, 695–702.

Ketchum C, Miller H, Song W, Upadhyaya A (2014). Ligand mobility regulates B cell receptor clustering and signaling activation. Biophys J 106, 26–36.

Ketchum CM, Sun X, Suberi A, Fourkas JT, Song W, Upadhyaya A (2018). Subcellular topography modulates actin dynamics and signaling in B-cells. Mol Biol Cell 29, 1732–1742.

Kwon KW, Park H, Doh J (2013). Migration of T cells on surfaces containing complex nanotopography. PLoS One 8, e73960.

Kwon KW, Park H, Song KH, Choi J-C, Ahn H, Park MJ, Suh K-Y, Doh J (2012). Nanotopography-guided migration of T cells. J Immunol 189, 2266 LP–2273.

Lam Hui K, Wang C, Grooman B, Wayt J, Upadhyaya A (2012). Membrane dynamics correlate with formation of signaling clusters during cell spreading. Biophys J 102, 1524–1533.

Lee K, Kim EH, Oh N, Tuan NA, Bae NH, Lee SJ, Lee KG, Eom C-Y, Yim EK, Park S (2016). Contribution of actin filaments and microtubules to cell elongation and alignment depends on the grating depth of micrograttings. J Nanobiotechnology 14, 35.

Lee R, Campanello L, Hourwitz M, Alvarez P, Omidvar A, Fourkas J, Losert W (2020). Quantifying topography-guided actin dynamics across scales using optical flow. Mol Biol Cell, mbc.E19-11-0614.

López MP, Huber F, Grigoriev I, Steinmetz MO, Akhmanova A, Koenderink GH, Dogterom M (2014). Actin–microtubule coordination at growing microtubule ends. Nat Commun 5, 4778.

Lou H-Y, Zhao W, Zeng Y, Cui B (2018). The Role of membrane curvature in nanoscale topography-induced intracellular signaling. Acc Chem Res 51, 1046–1053.

Lucas B, Kanade T (1981). an iterative image registration technique with an application to stereo vision (IJCAI).

Martín-Cófreces NB, Robles-Valero J, Cabrero JR, Mittelbrunn M, Gordón-Alonso M, Sung C-H, Alarcón B, Vázquez J, Sánchez-Madrid F (2008). MTOC translocation modulates IS formation and controls sustained T cell signaling. J Cell Biol 182, 951 LP–962.

Massey FJ (1951). The Kolmogorov-Smirnov test for goodness of fit. J Am Stat Assoc 46, 68–78.

Matov A, Applegate K, Kumar P, Thoma C, Krek W, Danuser G, Wittmann T (2010). Analysis of microtubule dynamic instability using a plus-end growth marker. Nat Methods 7, 761–768.

Mordechay L, Le Saux G, Edri A, Hadad U, Porgador A, Schvartzman M (2021). Mechanical regulation of the cytotoxic activity of natural killer cells. ACS Biomater Sci Eng 7, 122–132.

Mossman KD, Campi G, Groves JT, Dustin ML (2005). Altered TCR signaling from geometrically repatterned immunological synapses. Science (80-) 310, 1191 LP–1193.

Murugesan S, Hong J, Yi J, Li D, Beach JR, Shao L, Meinhardt J, Madison G, Wu X, Betzig E, et al. (2016). Formin-generated actomyosin arcs propel T cell receptor microcluster movement at the immune synapse. J Cell Biol 215, 383–399.

O'Connor RS, Hao X, Shen K, Bashour K, Akimova T, Hancock WW, Kam LC, Milone MC (2012). Substrate rigidity regulates human T cell activation and proliferation. J Immunol 189, 1330–1339.

Rey-Suarez I, Rogers N, Kerr S, Shroff H, Upadhyaya A (2021). Actomyosin dynamics modulate microtubule deformation and growth during T cell activation. Mol Biol Cell, mbc.E20-10-0685.

Ritter AT, Asano Y, Stinchcombe JC, Dieckmann NMG, Chen B-C, Gawden-Bone C, Engelenburg S, Legant W, Gao L, Davidson MW, et al. (2015). Actin depletion initiates events leading to granule secretion at the immunological synapse. Immunity 42, 864–876.

Saino E, Focarete ML, Gualandi C, Emanuele E, Cornaglia AI, Imbriani M, Visai L (2011). Effect of Electrospun Fiber Diameter and Alignment on Macrophage Activation and Secretion of Proinflammatory Cytokines and Chemokines. Biomacromolecules 12, 1900–1911.

Samelson LE, Patel MD, Weissman AM, Harford JB, Klausner RD (1986). Antigen activation of murine T cells induces tyrosine phosphorylation of a polypeptide associated with the T cell antigen receptor. Cell 46, 1083–1090.

El Shikh ME, El Sayed RM, Tew JG, Szakal AK (2007). Follicular dendritic cells stimulated by collagen type I develop dendrites and networks in vitro. Cell Tissue Res 329, 81–89.

Smoligovets AA, Smith AW, Wu H-J, Petit RS, Groves JT (2012). Characterization of dynamic actin associations with T-cell receptor microclusters in primary T cells. J Cell Sci 125, 735 LP–742.

Sun X, Driscoll MK, Guven C, Das S, Parent CA, Fourkas JT, Losert W (2015). Asymmetric nanotopography biases cytoskeletal dynamics and promotes unidirectional cell guidance. Proc Natl Acad Sci USA 112, 12557–12562.

Sun X, Hourwitz MJ, Baker EM, Schmidt BUS, Losert W, Fourkas JT (2018). Replication of biocompatible, nanotopographic surfaces. Sci Rep 8, 564.

Szakal AK, Gieringer RL, Kosco MH, Tew JG (1985). Isolated follicular dendritic cells: cytochemical antigen localization, Nomarski, SEM, and TEM morphology. J Immunol 134, 1349–1359.

Tabdanov ED, Puram V, Zhovmer A, Provenzano PP (2018). Microtubule-actomyosin mechanical cooperation during contact guidance sensing. Cell Rep 25, 328–338.e5.

Upadhyaya A (2017). Mechanosensing in the immune response. Semin Cell Dev Biol 71, 137–145.

Yi J, Wu X, Chung AH, Chen JK, Kapoor TM, Hammer JA (2013). Centrosome repositioning in T cells is biphasic and driven by microtubule end-on capture-shrinkage. J Cell Biol 202, 779 LP–792.

Yi J, Wu XS, Crites T, Hammer JA, Pollard TD (2012). Actin retrograde flow and actomyosin II arc contraction drive receptor cluster dynamics at the immunological synapse in Jurkat T cells. Mol Biol Cell 23, 834–852.

York AG, Chandris P, Nogare DD, Head J, Wawrzusin P, Fischer RS, Chitnis A, Shroff H (2013). Instant super-resolution imaging in live cells and embryos via analog image processing. Nat Methods 10, 1122.

Yu C, Wu H-J, Kaizuka Y, Vale RD, Groves JT (2010). Altered actin centripetal retrograde flow in physically restricted immunological synapses. PLoS One 5, e11878.

Zhao W, Hanson L, Lou H-Y, Akamatsu M, Chowdary PD, Santoro F, Marks JR, Grassart A, Drubin DG, Cui Y, et al. (2017). Nanoscale manipulation of membrane curvature for probing endocytosis in live cells. Nat Nanotechnol 12, 750–756.